Nano Energy (2016) **19**, 222–233

Available online at www.sciencedirect.com

ScienceDirect

journal homepage: www.elsevier.com/locate/nanoenergy

COMMUNICATION

3D self-supported nanopine forest-like Co_3O_4@$CoMoO_4$ core-shell architectures for high-energy solid state supercapacitors

Jing Wang[a], Xiang Zhang[b], Qiulong Wei[c], Haiming Lv[b], Yanlong Tian[b], Zhongqiu Tong[b], Xusong Liu[a], Jian Hao[a], Huiying Qu[a], Jiupeng Zhao[a], Yao Li[b,*], Liqiang Mai[c,*]

[a]*School of Chemical Engineering and Technology, Harbin Institute of Technology, Harbin 150001, PR China*
[b]*Center for Composite Materials and Structure, Harbin Institute of Technology, Harbin 150001, PR China*
[c]*State Key Laboratory of Advanced Technology for Materials Synthesis and Process, Wuhan University of Technology, Wuhan 430070, PR China*

Received 30 July 2015; received in revised form 18 October 2015; accepted 28 October 2015
Available online 10 November 2015

KEYWORDS
Co_3O_4@$CoMoO_4$;
Core-shell architecture;
Hydrothermal method;
Synergistic effect;
Solid-state supercapacitors;
Energy storage

Abstract
Herein, we develop a supercapacitor electrode composed of 3D self-supported Co_3O_4@$CoMoO_4$ core-shell architectures directly grown on nickel foam. Co_3O_4 nanocones are grown vertically on the nickel foam as the core and $CoMoO_4$ nanosheets are further engineered to immobilized on the surface of the nanocones as the shell. The unique architecture take advantage of a large interfacial area, numerous channels for rapid diffusion of electrolyte ions, fast electron transport and the high electrochemical activity from both the Co_3O_4 and $CoMoO_4$. The electrode exhibits high specific capacitance of 1902 F g^{-1} at current density of 1 A g^{-1}, good rate capability, and cycling stability with 99% capacitance retention after 5000 cycles. Solid-state asymmetric supercapacitor (Co_3O_4@$CoMoO_4$//CNTs) and symmetric supercapacitor (Co_3O_4@$CoMoO_4$//Co_3O_4@$CoMoO_4$) are fabricated with excellent electrochemical performance. The asymmetric supercapacitor with a maximum voltage of 1.6 V has demonstrated a high energy density of 45.2 W h kg^{-1}, a high power density of 6400 W kg^{-1} at 37.0 W h kg^{-1}, and outstanding cyclic stability with the capacitance retention of 98.5% after 3000 cycles.

*Corresponding authors.
E-mail addresses: yaoli@hit.edu.cn (Y. Li), mlq518@whut.edu.cn (L. Mai).

http://dx.doi.org/10.1016/j.nanoen.2015.10.036
2211-2855/

Introduction

With ever-increasing environmental pollution and the continuous demand for energy consumption, more efforts have been used to develop the sustainable and environmentally friendly alternative energy sources and energy storage devices [1-8]. Electrochemical capacitors (ECs), also called supercapacitors, have attracted tremendous interest due to their high power performance, fast recharge ability, long cycle life, non-pollution and low maintenance cost [9-12]. It is well known that ECs can provide instantaneously a higher power density than batteries and higher energy density than conventional capacitors [13-15]. Therefore, they have been widely used in portable electronics, electrical vehicles and various microdevices. The performance of ECs greatly depends on their electrode materials. Currently, many researches focus on the rational design of proper electrode with high capacity, large energy density and long cycling stability. Among them, numerous efforts have been made to investigate pseudocapacitive transition-metal-based oxides or hydroxides, because they can produce much higher specific capacitances than typical carbon-based electrochemical double-layer capacitors (EDLCs) and electronically conducting polymers [16-22].

Recently, considerable attention has been paid to the construction of intriguing hetero architectures of transition metal oxides or hydroxides for EC electrodes to boost the electrochemical performance. For example, Kong et al. [23] reported a cost-effective and simple strategy to design and fabricate Co_3O_4@MnO_2 hierarchical nanoneedle arrays on nickel foam, which presented a high capacitance of 1693.2 F g^{-1} at 1 A g^{-1} with long-term cycling stability for supercapacitors. Hercule et al. [24] prepared hierarchical nanostructured MoO_2/$Co(OH)_2$. The electrode exhibited a high capacitance of 800 F g^{-1} at 20 A g^{-1} with only 3% capacitance loss after 5000 cycles, which was better than those of individual component. Chen and his coworkers [13] reported a one step hydrothermal co-deposition method for the growth of ultrathin $Ni(OH)_2$-MnO_2 hybrid nanosheets arrays on nickel foam. The hybrid electrode showed ultra-high capacitance (2628 F g^{-1}) and energy density (81.2 W h kg^{-1}) in the three-electrode measurement. Luo et al. [25] reported a $ZnCo_2O_4$/MnO_2 nanocone with a mesoporous hierarchical core-shell structure, which exhibited exceptional specific capacitance of 1526 F g^{-1} at 10 A g^{-1} in the three electrode test, as well as achieving capacitance retention of 94.5% after 8000 cycles. These nanoarchitectured materials aforementioned have great superiorities as pseudocapacitive electrodes owing to their synergies resulting from the multistructure hybrid and integrating heterocomposites.

Co_3O_4 is an attractive pseudocapacitive material because of its great redox activity and extremely high theoretical specific capacitance (ca. 3560 F g^{-1}) [26-28]. However, Co_3O_4 suffers from poor capacity retention and rate capacity.

Binary transition metal oxides have been considered to be the promising candidates as electrodes for high performance pseudocapacitors due to their multiple redox reactions and high electrical conductivity. Among them, metal molybdates, such as $CoMoO_4$ is particularly attracted owing to its excellent rate capability and cycling ability, abundant sources and environmental friendliness. In our previous work, we have synthesized heterostructured $MnMoO_4$-$CoMoO_4$ nanowires, which exhibit a specific capacitance of 181.7 F g^{-1} at a current density of 1 A g^{-1} with good reversibility and cyclic efficiency [29]. Xia et al. synthesized $CoMoO_4$-graphene for supercapacitor applications, which showed a specific capacitance of about 394.5 F g^{-1} from the CV curve at 1 mV s^{-1}[30]. Unfortunately, up till now, the specific capacitance of $CoMoO_4$ reported is still undesirable for its widespread practical application [31,32]. This inspired us to design and fabricate an elegant Co_3O_4 and $CoMoO_4$ heterostructured electrode, which will combine the merits of both Co_3O_4 and $CoMoO_4$, together with the well-designed architecture to improve the performance. It is worth noting that Gu et al., prepared Co_3O_4@$CoMoO_4$ core/shell nanowire arrays by hydrothermal ion exchange method [33]. In their work, Co_3O_4 nanowires coated with $CoMoO_4$ nanofilms were constructed and the electrode exhibited the specific capacitance of 1040 F g^{-1} at a current density of 1 A g^{-1}, and the symmetric supercapacitor device was studied in liquid electrolyte. To the best of our knowledge, solid-state supercapacitor applications for the Co_3O_4@$CoMoO_4$ electrode have never been explored.

Herein, we for the first time reported that 3D self-supported Co_3O_4@$CoMoO_4$ core-shell nano-pine forest (NPF) arrays were directly grown on the conductive current collector using a facile stepwise hydrothermal method. Co_3O_4 nanocones (NCs) were grown on the nickel foam as the core and $CoMoO_4$ nanosheets (NSs) were further firmly attached to the NCs as the shell to form a 3D self-supported Co_3O_4@$CoMoO_4$ core-shell arrays. Such unique architecture can offer a large interfacial area for reaction, numerous channels for rapid diffusion of electrolyte ions, and fast electron transport, which endows the designed Co_3O_4@$CoMoO_4$ NPF electrode with an excellent capacitive performance. The as prepared Co_3O_4@$CoMoO_4$ core-shell electrode exhibits a high specific capacitance of 1902 F g^{-1}, which is much higher than that of Gu et al. reported (1040 F g^{-1} at 1 A g^{-1}) [33]. Good rate capability and excellent long-term cycling performance are also demonstrated in such a hybrid electrode. In addition, solid state asymmetric and symmetric supercapacitor devices fabricated by using our Co_3O_4@$CoMoO_4$ NPF as electrodes have demonstrated a high energy density of 45.2 W h kg^{-1}, a high power density of 6400 W kg^{-1} at 37.0 W h kg^{-1}, and outstanding cyclic stability with the capacitance retention of 96.5% after 3000 cycles at a current density of 0.5 A g^{-1}. This study constitutes a promising strategy toward design and fabrication of transition metal oxides based nanostructured cathode with good energy storage performance for supercapacitors.

Experimental details

All of the reagents used in the experiments were of analytical grade and were used without further purification. Prior to the synthesis, the Ni foam ($1 \times 1 \times 0.1$ cm^3) was cleaned by sonication in the acetone, ethanol and deionized water in sequence for 30 min, respectively. Co_3O_4 NCs,

$CoMoO_4$ NSs and Co_3O_4@$CoMoO_4$ NPF were prepared by the hydrothermal method.

Synthesis of Co_3O_4 nanocones

The pristine Co_3O_4 NCs were synthesized on nickel foam by a hydrothermal method. In a typical synthesis, 1.18 g $CoCl_2 \cdot 6H_2O$ and 1.80 g urea were dissolved in 60 ml deionized water under constant magnetic stirring for 2 h. The solution was then transferred to a 100 ml Teflon-lined stainless steel autoclave, with a piece of Ni foam immersed in the reaction solution. The autoclave was sealed and maintained at 120 °C for 10 h and then cooled to room temperature. Then the samples were dried at 60 °C for 12 h, followed by annealing at 200 °C in air for 1 h to obtain Co_3O_4 NCs.

Synthesis of $CoMoO_4$ nanosheets

In a typical synthesis, 0.14 g $CoCl_2 \cdot 6H_2O$ and 0.15 g $Na_2MoO_4 \cdot 7H_2O$ were dissolved in 50 ml deionized water under constant magnetic stirring. The $CoMoO_4$ precursor solution was transferred to a 100 ml Teflon-lined stainless steel autoclave, with a piece of pretreated Ni foam immersed in the reaction solution. The autoclave was sealed and maintained at 180 °C for 10 h and then cooled to room temperature. The sample of $CoMoO_4$ NSs was then rinsed and dried at 60 °C for 12 h.

Synthesis of Co_3O_4@$CoMoO_4$ nanopine forest

In a typical synthesis, the as obtained Co_3O_4 NCs on Ni foam were immersed into the precursor solution of $CoMoO_4$. Then they were transferred to a 100 ml Teflon-lined stainless steel autoclave. The autoclave was sealed and maintained at 180 °C for 10 h and then cooled to room temperature. The as prepared Co_3O_4@$CoMoO_4$ NPF was rinsed and dried at 60 °C for 12 h.

Preparation of carbon nanotubes (CNTs) electrode

The CNTs were pretreated firstly as follows: 1 g CNTs was mixed with 200 ml 68% HNO_3, then was heated at 80 °C for 24 h with constant stirring. Then the CNTs were rinsed and dried at 60 °C for 12 h. The negative electrode for the asymmetric supercapacitors was prepared by mixing CNTs (80 wt%) with carbon black (10 wt%) and polyvinylidenefluoride (PVDF, 10 wt%). A small amount of N-methylpyrrolidone (NMP) was then added to form a homogeneous mixture. The resulting mixture was coated onto a 1 cm^2 Ni-foam and was dried at 80 °C for 12 h.

Materials characterizations

Scanning electron microscopy (SEM) images were collected with a Hitachi S-4800 at an acceleration voltage of 20 kV. Transmission electron microscopy (TEM) images, high-resolution transmission electron microscopy (HRTEM) images, and selected-area electron diffraction (SAED) patterns were recorded by using TEM (JEOL JEM-2010). The structures of the samples were characterized by X-ray diffraction (XRD, Rigaku D/max-rB, Cu Kα radiation, λ=0.1542 nm, 40 kV,100 mA). Brunauer–Emmett–Teller (BET) analysis was carried out to evaluate the surface area and pore size distribution of the as prepared products. Surface Area Analyzer (NOVA2000E) was used to measure N_2-sorption isotherm.

Electrochemical measurements

Electrochemical measurements were performed on an electrochemical workstation (CHI 660D, Shanghai,China) using a three-electrode mode in a 2 M KOH aqueous solution within the potential window of −0.2 to 0.6 V. The nickel foam supported Co_3O_4@$CoMoO_4$ NPF (~1 cm^2 area; Co_3O_4@$CoMoO_4$ mass: 3.3 mg) or pristine Co_3O_4 NCs (mass: 2.5 mg) or $CoMoO_4$ NSs (mass: 1.1 mg) acted directly as the working electrodes. A platinum electrode and a saturated calomel electrode (SCE) served as the counter electrode and the reference electrode, respectively. Electrochemical impedance spectroscopy (EIS) measurements were carried out by applying an alternating voltage with 5 mV amplitude in a frequency range from 0.1 Hz to 100 kHz at open circuit potential. The specific capacitance, energy density and power density were calculated from the following equations:

$$C_s = \frac{I\Delta t}{m\Delta V} \quad (1)$$

$$E = \int UdQ = \int UIdt = I\int Udt \quad (2)$$

$$P = \frac{3600E}{\Delta t} \quad (3)$$

where C_s (F g^{-1}) is the specific capacitance, I (A) is the constant discharge current, Δt (s) is the discharge time, ΔV (V) is the potential drop during discharge process, m (g) is the mass of the active materials, $\int Udt$ is the enclosed area of the discharge curve and coordinate axis, U (V) is the potential window of the supercapacitor devices, t (s) is the corresponding discharge time of the devices. E (W h kg^{-1}) is the energy density, and P (W kg^{-1}) is the power density.

Preparation and characterization of the solid state asymmetric and symmetric supercapacitors

The asymmetric supercapacitors were assembled by using Co_3O_4@$CoMoO_4$ NPF as the positive electrode, CNTs as the negative electrode with a separator and PVA/KOH as a solid electrolyte. Each electrode had a geometric surface area of 1 cm^2. PVA/KOH gel was prepared by mixing 5.6 g KOH with 6 g PVA in 50 ml deionized water and heated at 80 °C under stirring for 4 h. The electrodes and the separator were soaked in the gel for 5 min, then taken out from the gel, and assembled together. The device was placed in the air for 24 h and became solid. The electrochemical performance of the asymmetric supercapacitor was tested by an electrochemical workstation (CHI 660D, Shanghai, China) using a two-electrode mode.

The symmetric supercapacitors consisted of Co_3O_4@$CoMoO_4$ NPF as both the positive electrode and the negative electrode with PVA/KOH as the solid electrolyte were

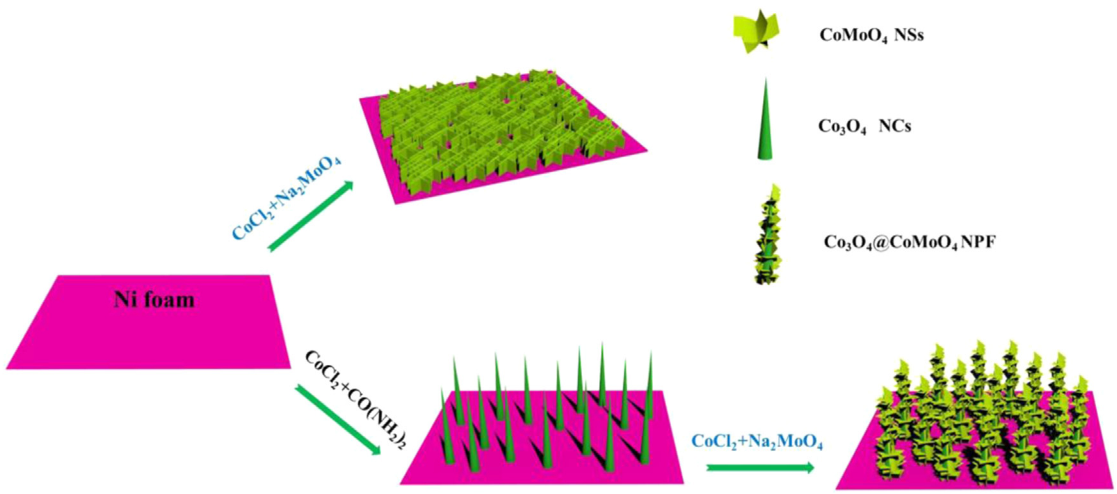

Figure 1 Schematic illustration for the fabrication of 3D self-supported Co_3O_4@$CoMoO_4$ NPF arrays.

fabricated and tested by an electrochemical workstation (CHI 660D, Shanghai, China) using a two-electrode mode.

Results and discussion

The schematic procedure for the fabrication of the 3D self-supported Co_3O_4@$CoMoO_4$ NPFs architecture is illustrated in Figure 1. First, commercial nickel foam is employed as the current collector for the preparation of Co_3O_4 NCs via hydrothermal route. Then $CoMoO_4$ NSs is further immobilized on the nanocone arrays through the hydrothermal process to form the Co_3O_4@$CoMoO_4$ NPF arrays. The optical images of the as prepared electrodes are shown in Figure S1. The morphology of the Co_3O_4 NCs is shown in Figure 2a, which clearly reveals that a large amount of nanocones with uniform structure are observed. The nanocones have an average bottom diameter of 150 nm and length of around 2 μm.

Figure 2b shows the SEM image of $CoMoO_4$ which possesses a nanostructure composed of nanosheets with an average thickness of 20 nm. The nanosheets are interconnected with each other and form a network structure with highly porous configuration. Figure 2c shows that large-scale and aligned Co_3O_4@$CoMoO_4$ nanopines grow uniformly on the surface of the Ni foam. The numerous Co_3O_4@$CoMoO_4$ nanopines appear like "nanopine forest", standing vertically on the Ni foam (Figure 2d). The high magnification SEM (inset of Figure 2d) clearly demonstrates that $CoMoO_4$ NSs are homogeneously covered on the whole surface of Co_3O_4 NCs and form the 3D Co_3O_4@$CoMoO_4$ core/shell arrays. The vertical self-supported arrays and the interconnected shells are beneficial to the fast ion and electron transportation, and the porous nanostructure facilitates electrolyte infiltration. Brunauer–Emmett–Teller (BET) analysis results show that the specific surface area of Co_3O_4@$CoMoO_4$ NPF is 61.4 $m^2\,g^{-1}$, which is much higher than that of Co_3O_4 NCs (40.2 $m^2\,g^{-1}$) and $CoMoO_4$ NSs (55.6 $m^2\,g^{-1}$) (Figure S2). This core/shell configuration can provide a higher surface area, which is mainly attributed to the interconnected $CoMoO_4$ NSs and the aligned Co_3O_4 NCs scaffold that creating a 3D structure and highly porous surface morphology. Such configuration is of great importance to promote electrolytes accessibility and increase the utilization of the active materials [34-39]. The zone labeled with red line in Figure 2d is selected to research the Energy Dispersive X-ray Spectroscopy (EDS) and SEM mapping (Figure S3). It can be clearly seen that only elements of O, Co, and Mo could be found in the Co_3O_4@$CoMoO_4$ NPF.

The crystallinity and crystal phases of the as-prepared samples were examined by X-ray diffraction (XRD) and the results are shown in Figure S4. The patterns of Co_3O_4 NCs and $CoMoO_4$ NSs are in good agreement with the standard patterns for the cubic phase of Co_3O_4 (PDF, card No. 42-1467) and monoclinic $CoMoO_4$ (PDF, card No. 21-0868), respectively. Besides the diffraction peaks of monoclinic $CoMoO_4$, several weak diffraction peaks attributed to $CoMoO_6 \cdot 0.9H_2O$ are observed. The patterns of Co_3O_4@$CoMoO_4$ NPF contain the diffraction peaks of both Co_3O_4 and $CoMoO_4$, indicating the presence of both phases.

The typical TEM and HRTEM images of Co_3O_4 NCs are displayed in Figure 3a and b. The lattice fringes show the lattice spacing is 0.47 nm, which is corresponding to the (111) planes of the cubic Co_3O_4. The SEAD in Figure 3b reveals that the Co_3O_4 NCs are polycrystalline structure. Figure 3c and d shows TEM and HRTEM images of Co_3O_4@$CoMoO_4$ core/shell structure. It is evidently observed that the Co_3O_4 NCs are coated with $CoMoO_4$ NSs, forming a typical core-shell heterostructure. HRTEM reveals that the shell has a visible lattice fringes of 0.33 nm and 0.30 nm, corresponding well to the (002) and (310) planes of $CoMoO_4$, respectively. The SEAD pattern in Figure 3d indicates the polycrystalline characteristics of the Co_3O_4@$CoMoO_4$ NPF. TEM image and EDS mapping of the Co_3O_4@$CoMoO_4$ sample (Figure S5) further indicate that the elements of Co and O are distributed uniformly on both the core and the shell, while there are more Mo elements in the shell of the nanopine. The mapping results are in well accordance with the fact that the sample has a core consisting of Co_3O_4 and a shell consisting of $CoMoO_4$.

To investigate the potential application of the unique Co_3O_4@$CoMoO_4$ NPF as supercapacitor electrodes, the electrochemical performances of the as-prepared products are tested in a three-electrode system with a 2 M KOH solution

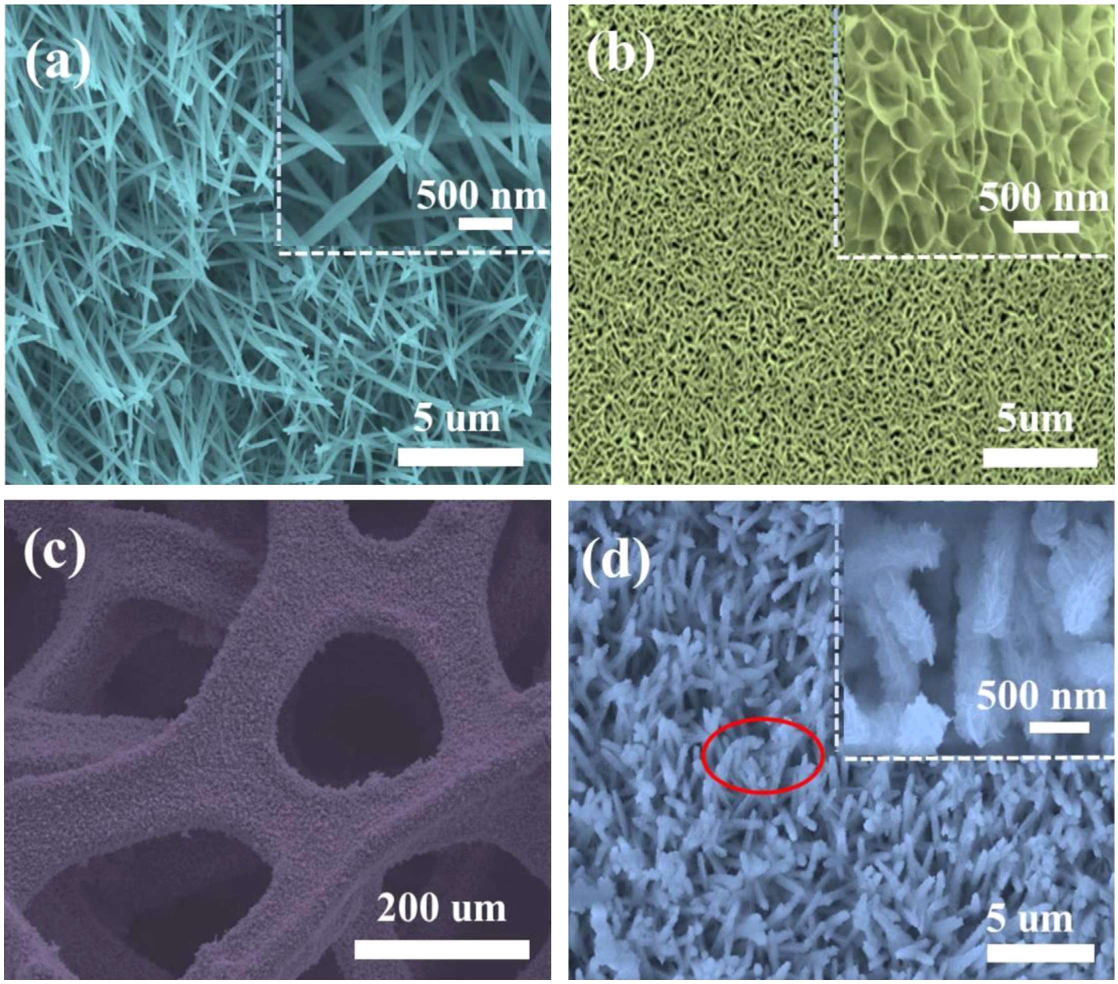

Figure 2 SEM images of (a) Co_3O_4 NCs on nickel foam, the inset is the high magnification SEM image; (b)$CoMoO_4$ NSs on nickel foam. The inset is the magnified view. (c) Co_3O_4@$CoMoO_4$ NPF on nickel foam. (d) Co_3O_4@$CoMoO_4$ NPF taken at different magnifications.

as the electrolyte. Figure 4a compares the cyclic voltammetry (CV) curves of the pristine Co_3O_4 NCs, $CoMoO_4$ NSs and Co_3O_4@$CoMoO_4$ NPF at a scan rate of 5 mV s^{-1}. Well-defined redox peaks within −0.2 to 0.6 V are visible on the CV curves of these oxide electrodes, indicating the strong pseudocapacitive nature of the electrodes. As expected, the area for Co_3O_4@$CoMoO_4$ NPF, compared with that of the Co_3O_4 NCs and the $CoMoO_4$ NSs electrodes, shows an obvious increase, further indicating that the core-shell electrode possesses a significantly higher specific capacitance and higher electrochemical activity than individual component, arising from the increased surface area and structural effect from the 3D hybrid structure of Co_3O_4 NCs and $CoMoO_4$ NSs. To check the substrate effect of Ni foam, the CV curve of Ni foam is also presented. Evidently, the Ni foam contributes very little to the total capacitance of the electrode.

The rate capability of the Co_3O_4@$CoMoO_4$ NPF electrode was also investigated by measuring the CV curves at different scan rates and charging-discharging curves at different current densities, as shown in Figure 4b and c. (See Supporting information Figure S6, the comparative CVs and charging-discharging curves of Co_3O_4 NCs and $CoMoO_4$ NSs performed in a three-electrode cell). All the CV curves show obvious pseudocapacitance features with a similar line-type and the curves keep the original shape with the increasing scan rates, indicating of the desirable fast ionic and electron transportation of the electrodes. The peak current increases with the increase of the scan rate, suggesting the good reversibility of the fast charge-discharge response of the electrode. The galvanostatic charge-discharge curves of Co_3O_4@$CoMoO_4$ NPF electrode tested at current density of 0.5-10 A g^{-1} (Figure 4c) show that each curve has a good symmetry, implying excellent electrochemical reversibility and charge-discharge properties. The specific capacitance of the Co_3O_4@$CoMoO_4$ NPF electrode calculated from the discharge curves according to Eq. (1) are 1902, 1760, 1506, 1350, 1280, and 1200 F g^{-1} at current densities of 1, 2, 3, 5, 8, and 10 A g^{-1}, respectively. The specific capacitances of the three electrodes derived from the discharging curves at different current densities are compared, as shown in Figure 4d. The results reveal that the Co_3O_4@$CoMoO_4$ NPF electrode exhibits a much higher capacitance than that of Co_3O_4 NCs and $CoMoO_4$ NSs. Even at current density as high as 10 A g^{-1}, the Co_3O_4@$CoMoO_4$ electrode still delivers a high specific capacitance of 1200 F g^{-1}, indicating its superior rate capability.

To gain further insight into the advantages of the Co_3O_4@$CoMoO_4$ NPF electrode, the electrochemical

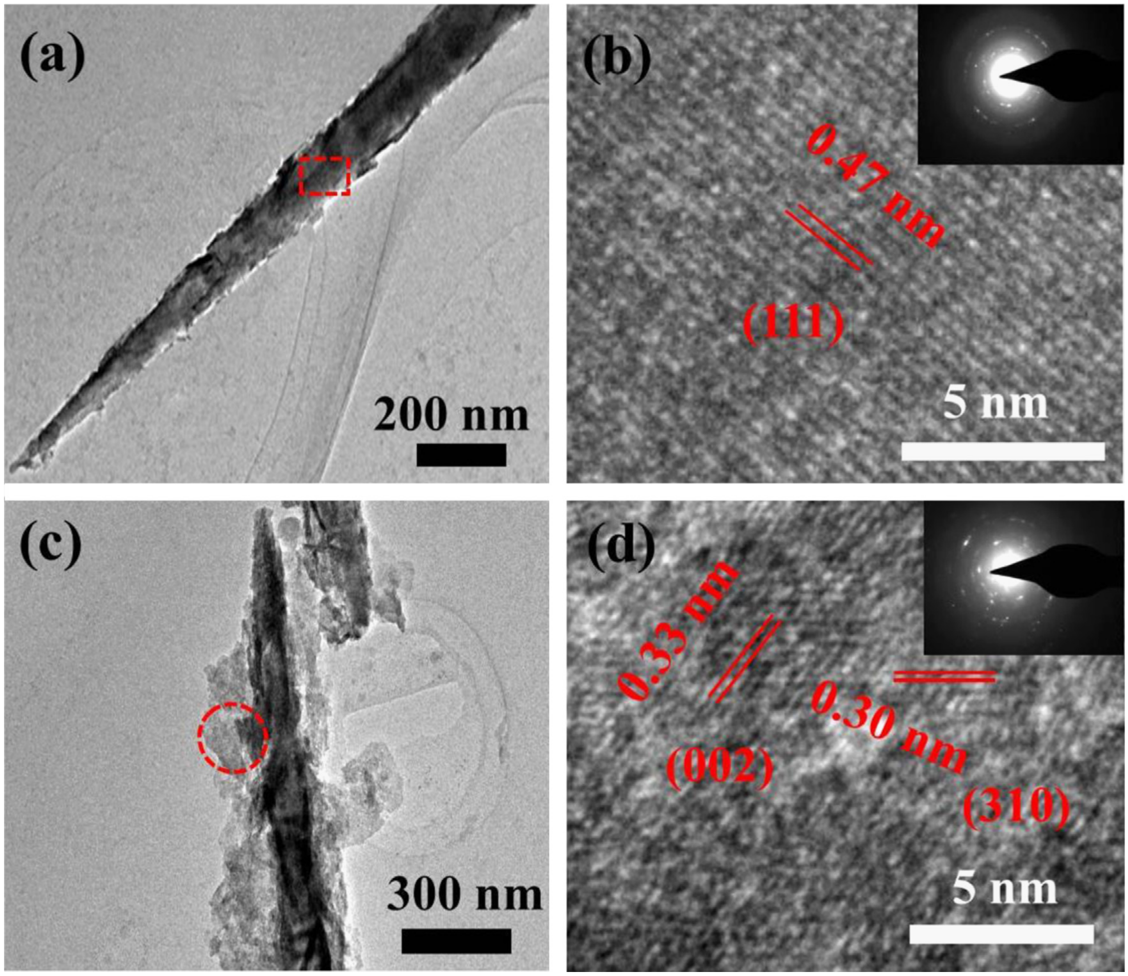

Figure 3 (a) TEM image of an individual Co_3O_4 NC; (b) HRTEM image of the Co_3O_4 NC and corresponding SAED pattern; (c) TEM image of the Co_3O_4@$CoMoO_4$ core/shell structure; (d) HRTEM image of the Co_3O_4@$CoMoO_4$ core-shell structure and corresponding SAED pattern.

impedance spectra (EIS) were tested. The Nyquist plots of the pristine Co_3O_4 NCs, $CoMoO_4$ NSs and Co_3O_4@$CoMoO_4$ NPF are shown in Figure 4e. The inset shows the semicircle at high frequency. The shapes of the impedance spectra are similar, being composed of one quasi-semicircle at high frequency followed by a linear component at low frequency. From the point intersecting with the real axis in the high frequency, the Co_3O_4@$CoMoO_4$ NPF electrode demonstrates a much smaller internal resistances (0.76 Ω) compared with that of Co_3O_4 NCs (1.67 Ω) and $CoMoO_4$ NSs (1.29 Ω), indicative of improved electrical conductivity. Moreover, the Co_3O_4@$CoMoO_4$ NPF electrode demonstrates the smallest charge-transfer resistance and diffusive resistance. The above results show that the combination of fast ion diffusion as well as low electro-transfer resistance is also responsible for the enhanced electrochemical performance of the Co_3O_4@$CoMoO_4$ core/shell electrode.

The cycling performance of the three electrodes was evaluated at a current density of 3 A g^{-1}, as shown in Figure 4f. It shows that the Co_3O_4@$CoMoO_4$ NPF electrode exhibits an excellent long-term electrochemical stability and the capacitance loss after 3000 cycles is only 1.5%. By contrast, the capacitance retentions are 85.7% and 91.7% for Co_3O_4 NCs and $CoMoO_4$ NSs, respectively.

We further performed a charge-discharge cycling test at a current density of 5 A g^{-1} to examine the long-term cyclability of Co_3O_4@$CoMoO_4$ NPF (Figure 5a), which indicates that the charge-discharge process of the electrode is highly reversible. The specific capacitance of Co_3O_4@$CoMoO_4$ NPF electrode at 5 A g^{-1} changes from 1350 F g^{-1} of the first cycle to 1337 F g^{-1}, which keeps 99% capacitance retention after 5000 cycles. Typical Nyquist plots of the Co_3O_4@$CoMoO_4$ electrode after the 1st and 5000th cycles are presented in Figure 5b. The arc increment from the 1st to the 5000th cycles is not so obvious, indicating that the nanostructures are well maintained and preserved overall with little structural deformation after 5000 cycles. In addition, the increase of the Warburg resistance after 5000 cycles can be attributed to the loss of adhesion of some active materials blocking the diffusion pathways of ions during the charge-discharge process.

Figure 5c demonstrates the different current densities dependent cycling performance. During the first 100 cycles with a charge-discharge density of 10 A g^{-1}, the electrodes shows a stable specific capacitance of 1200 F g^{-1}. In the following 500 cycles, the charge-discharge rate changes successively and the electrode demonstrates the stable capacitance. After 600 cycles, with the current density

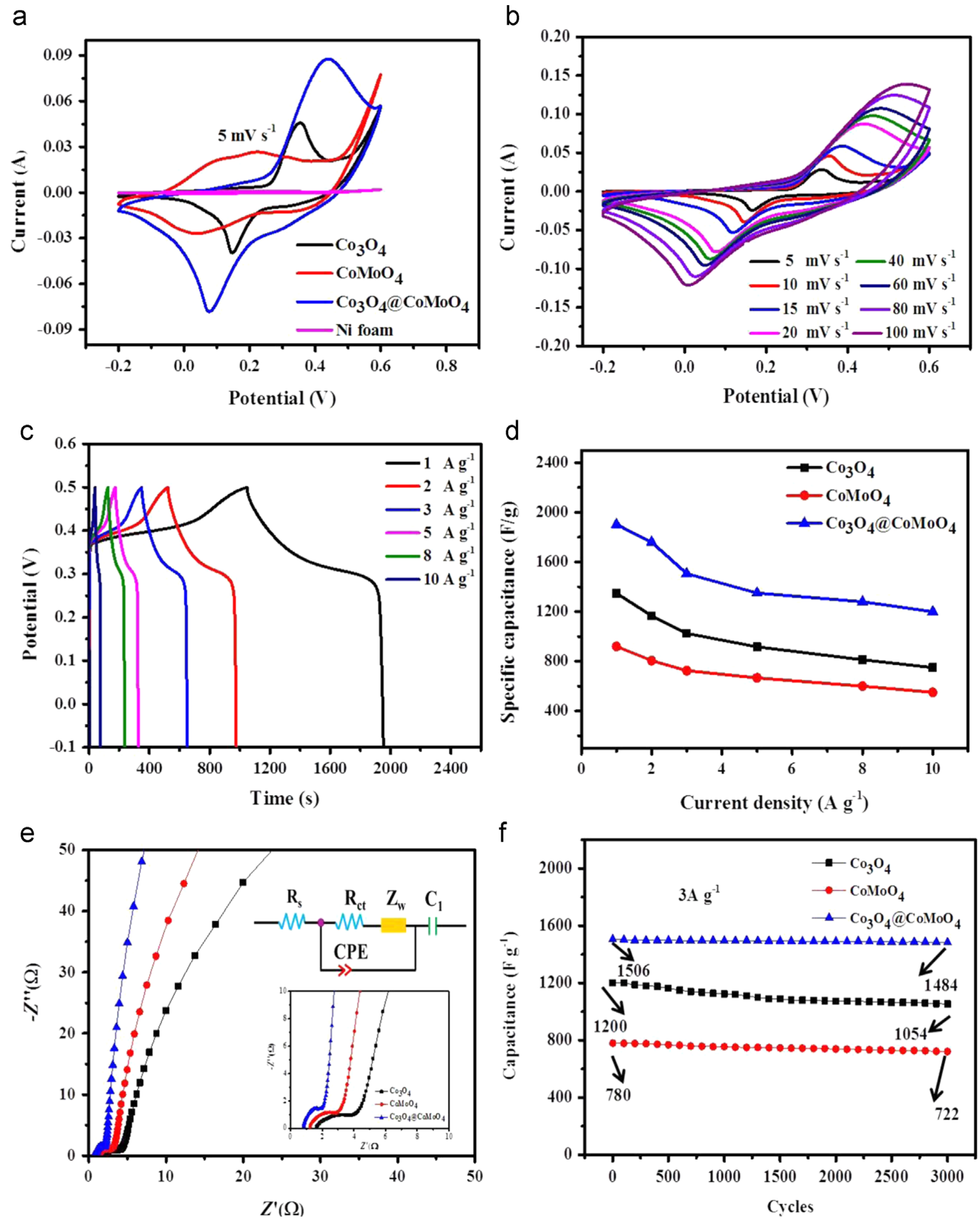

Figure 4 (a) CV curves of the pristine Co_3O_4 NCs, $CoMoO_4$ NSs and Co_3O_4@$CoMoO_4$ NPF at a scan rate of 5 mV s^{-1}; (b) CV curves of Co_3O_4@$CoMoO_4$ NPF at the scan rate between 5 and 100 mV s^{-1}; (c) charge and discharge curves of Co_3O_4@$CoMoO_4$ NPF at different current densities ranged from 0.5 to 10 A g^{-1}; (d) plots of the current density against specific capacitances of the Co_3O_4 NCs, $CoMoO_4$ NSs and Co_3O_4@$CoMoO_4$ NPF electrodes obtained from the galvanostatic charge-discharge curves; (e) Nyquist plots of Co_3O_4 NCs, $CoMoO_4$ NSs and Co_3O_4@$CoMoO_4$ NPF; (f) cycling performance of Co_3O_4 NCs, $CoMoO_4$ NSs and Co_3O_4@$CoMoO_4$ NPF at a discharge current density of 3 A g^{-1}.

back to 10 A g^{-1} for another 100 cycles, the capacitance of 1196 F g^{-1} can be recovered and without noticeable decrease, demonstrating the excellent rate capability and cycling stability. Such excellent cycling stability of the Co_3O_4@$CoMoO_4$ NPF is mainly attributed to the porous configuration of the core-shell arrays and the synergistic effect between Co_3O_4 and $CoMoO_4$.

In order to further demonstrate the advantage of the electrode, the Co_3O_4@$CoMoO_4$ NPF on nickel foam underwent bending for electrochemical test (Figure S7). Even

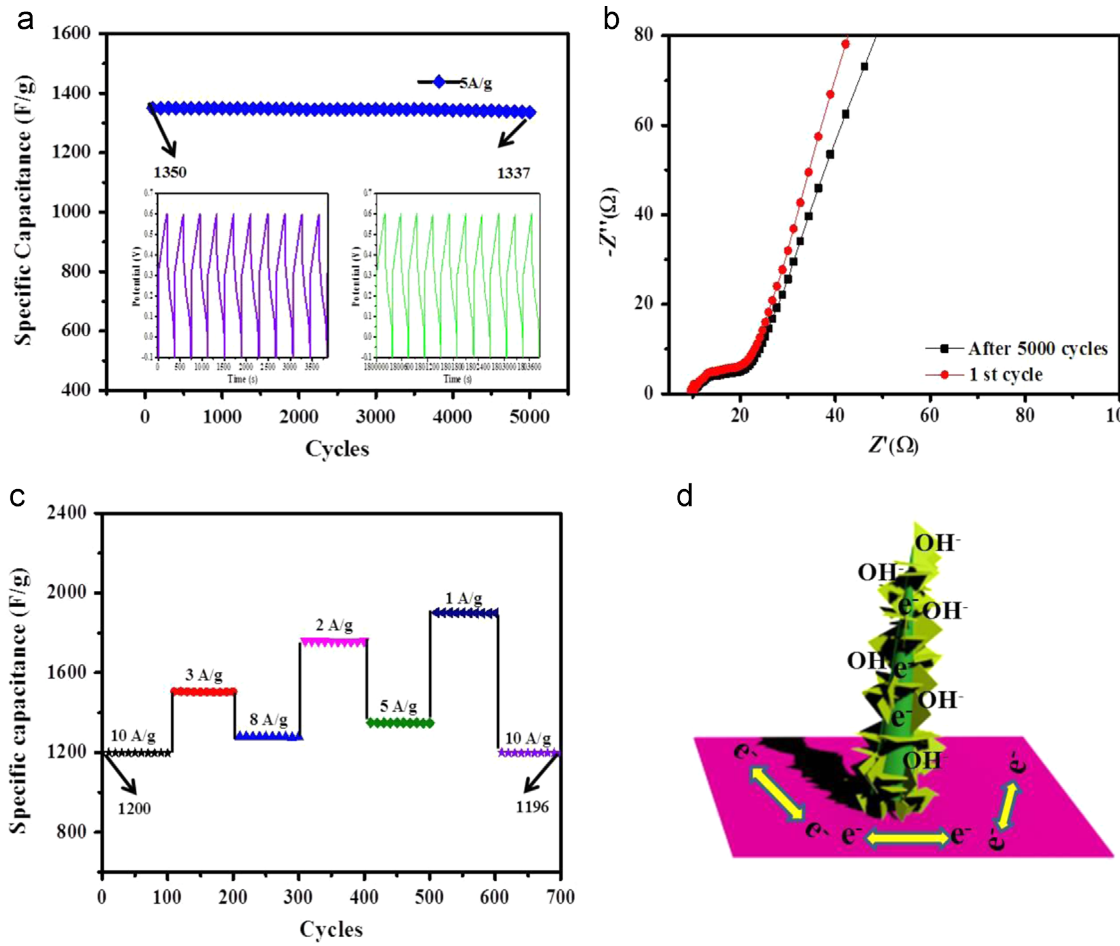

Figure 5 (a) Cycling performance of the Co_3O_4@$CoMoO_4$ NPF electrode based ECs at a discharge current density of 5 A g^{-1}. The inset is charge-discharge curve at a current density of 5 A g^{-1} after thousands of cycles; (b) Nyquist plots of the first and the 5000th cycles for the Co_3O_4@$CoMoO_4$ NPF electrode; (c) Rate performance and cycling stability of Co_3O_4@$CoMoO_4$ NPF under different current densities. (d) Schematic diagram of ion and charge transfer in the Co_3O_4@$CoMoO_4$ NPF electrode.

under bending angle of 0°, 180° and 360°, the CV curves of the Co_3O_4@$CoMoO_4$ NPF have almost no obvious changes, confirming that the 3D self-supported Co_3O_4@$CoMoO_4$ NPF electrode has a remarkable mechanical flexibility.

The high specific capacitance, enhanced rate capability and excellent cycling stability of the 3D Co_3O_4@$CoMoO_4$ core-shell NPF electrode are impressive values when compared to those of many previously reported $CoMoO_4$ or Co_3O_4 oxides based electrodes, as shown in Table S1.

The enhanced specific capacitance and superior electrochemical stabilities of the 3D Co_3O_4@$CoMoO_4$ NPF electrode are obviously attributed to the following features: First, as schematically demonstrated in Figure 5d, the longitudinally grown Co_3O_4 NCs serve as the backbone and conductive pathway, providing efficient charge transport for Faradic reaction and robust support for the structural integrity. Second, the ultrathin, interconnected and porous $CoMoO_4$ NSs are grown and well dispersed on the Co_3O_4 NCs, significantly enhancing the surface area of the electrode, making the structure accessible to electrolytes to a larger extent and providing more active sites for the adsorption of ion into the electrode during charge and discharge process. Third, the combination of Co_3O_4 and $CoMoO_4$ with the unique 3D architecture can substantially enhance their electrochemical properties. Both the Co_3O_4 core and $CoMoO_4$ shell are good pseudocapacitive materials with great redox activity, rich polymorphism and reversible charge storage [40-42], contributing to the total capacitance [38-40]. The good rate capability, excellent cycling ability and high electrical conductivity of $CoMoO_4$, together with the high specific capacitances of Co_3O_4 definitely lead to significantly improved electrochemical performance due to the synergistic effects.

To further demonstrate the feasibility of the 3D Co_3O_4@-$CoMoO_4$ NPF electrode for real application, solid-state asymmetric and symmetric supercapacitors storage devices were assembled and tested. The asymmetric supercapacitor (ASC) was made by using Co_3O_4@$CoMoO_4$ NPF as the cathode and the CNTs on Ni foam as the anode. The SEM images of CNTs electrode indicates that CNTs uniformly distribute on the skeleton of Ni foam (Figure S8). The charge-discharge curves of the CNTs within a potential window of −1 to 0 V at various current densities are observed in Figure S9. Prior to assembling the device, the charge between the Co_3O_4@$CoMoO_4$ NPF cathode and the CNTs anode needed to be optimized, and the optimal mass ratio between these two electrodes

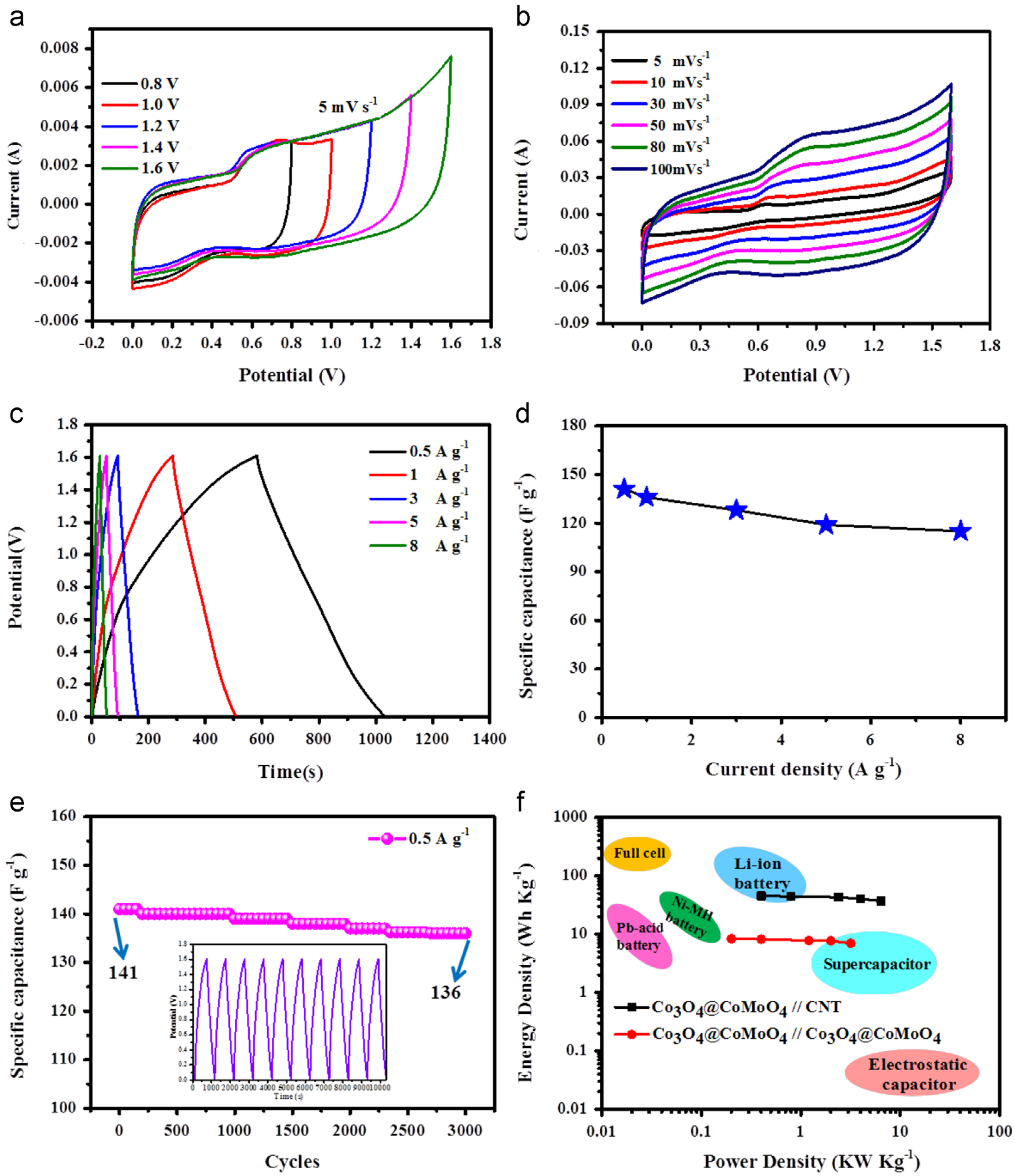

Figure 6 (a) CV curves of the optimized Co_3O_4@$CoMoO_4$ NPF//CNTs ACS device collected at different potential windows at a scan rate of 5 mV s^{-1}; (b) CV curves of the optimized Co_3O_4@$CoMoO_4$ NPF//CNTs ACS device collected at various scan rates; (c) charge-discharge curves of optimized Co_3O_4@$CoMoO_4$ NPF//CNTs ACS device collected at various current densities; (d) plot of the current density against the specific capacitance of Co_3O_4@$CoMoO_4$ NPF//CNTs ACS device; (e) cycling performance of Co_3O_4@$CoMoO_4$ NPF//CNTs ACS device at a discharge current density of 0.5 A g^{-1}. The inset is part of charge-discharge curves at a current density of 0.5 A g^{-1} after the 10th cycles; (f) the Ragone plots relating power density to energy density of asymmetric and symmetric supercapacitor devices.

was calculated to be 8:1, on the basis of the specific capacitance values and potential windows found for the Co_3O_4@$CoMoO_4$ NPF and the CNTs (Figure S10a). Figure 6a shows the CV curves of the Co_3O_4@$CoMoO_4$ NPFs//CNTs ACS device collected at 5 mV s^{-1} with an operational voltage window ranging from 0.8 to 1.6 V, indicating that the device is stable up to an optimal voltage of 1.6 V. The device reveals a typical capacitive behavior with nearly the rectangular CV curves and good stabilities at different potential windows, even at the potential window up to 1.6 V.

Figure 6b displays the CV curves of the Co_3O_4@$CoMoO_4$ NPFs//CNTs ASC device recorded at various scan rates. Unlike the apparent redox peaks observed in the CV curve of the Co_3O_4@$CoMoO_4$ NPFs electrode, all the CV curves exhibit quasi-rectangular shapes that are indicative of typical capacitive characteristics. Additionally, when the scan rate is increased, the shapes of the CV curves remain the same, indicating the desirable fast charge/discharge property for power devices.

The galvanostatic charge and discharge measurements were researched at various current densities (Figure 6c). Discharge curves are almost symmetrical to its corresponding charge curves, indicating good capacitive behavior for the asymmetric supercapacitor. As shown in Figure 6d, the Co_3O_4@$CoMoO_4$ NPF//CNTs ASC device achieves a specific capacitance of 128 F g^{-1} at a discharge current density of 3 A g^{-1}, which is higher than that of previously reported ASCs, such as ultrathin $CoMoO_4$ nanosheets modified with chitosan (81 F g^{-1} at 3 A g^{-1}). To our knowledge, 128 F g^{-1} is the best capacitance at a current density 3 A g^{-1} which has never been reported for $CoMoO_4$ vs CNT cell [43]. Furthermore, the Co_3O_4@$CoMoO_4$ NPF//CNTs ASC device retains a prominent rate capability of 81.5% at a high discharge current density of 8 A g^{-1}. The cycling durability of the ACS device is further evaluated at a current density of 0.5 A g^{-1} for 3000 cycles and it is seen that the device retains 98.5% of the initial capacitance, revealing its excellent long-term cyclic stability (Figure 6e). The excellent cycling stability of the solid state Co_3O_4@$CoMoO_4$ NPF//CNTs ASC device has considerably exceeded those previously reported ACSs, such as a 22% loss for the $CoMoO_4$//AC [43], a 36.4% loss for the $Ni(OH)_2$//active carbon (AC) [44], and a 33% loss for the $Ni(OH)_2$/CNT//AC [45].

Figure S11a shows the CV curves of Co_3O_4@$CoMoO_4$//Co_3O_4@$CoMoO_4$ symmetric supercapacitor (SSC) device at various scan rates within a potential range of 0-0.8 V. The redox peaks are visible in all CV curves, which is mainly attributed to the Faradaic redox. The charge-discharge curves of the SSC device at various current densities are further illustrated in Figure S11b. The discharge curve is asymmetrical to its corresponding charge curve due to the faradaic pseudocapacitance performance. The specific capacitances of the Co_3O_4@$CoMoO_4$//Co_3O_4@$CoMoO_4$ SSC device calculated from the discharge curves at current densities of 0.5, 1, 3, 5 and 8 A g^{-1} are 107, 93, 85, 71, and 68 F g^{-1}, respectively. Figure S11d reveals that the SSC device can retains about 96% of its initial capacitance after 3000 cycles, indicating the excellent capacitance durability.

The asymmetric capacitor exhibits a higher capacity than that of the symmetric one, which is mainly attributed to the lower capacitive activity of Co_3O_4@$CoMoO_4$ NPF when used as the negative electrode compared with CNTs. (See Figure S12 in Supporting information, the CV curves of the Co_3O_4@$CoMoO_4$ NPF electrode measured at different potential windows).

To demonstrate the operational characteristics, the energy densities of the supercapacitor devices at different average power density were calculated from the discharge curves according to Eqs. (2) and (3) [46]. Ragone plots relating power density to energy density of the ASC and SSC are demonstrated in Figure 6f. Our ASC device displays a high energy density of 45.2 W h kg^{-1} at a power density of 400 W kg^{-1}, approaching that of lithium ion batteries. Even at a high power density of 6400 W kg^{-1}, the device still has an energy density of 37.0 W h kg^{-1}, much superior to that of supercapacitors at the same power level. The ASC device could power a 5 mm diameter red light-emitting diode (LED) light, as shown in Figure S13.

Our results demonstrate the importance and great potential application of 3D self-supported Co_3O_4@$CoMoO_4$ core-shell NPF in the development of high performance energy storage systems.

Conclusion

In summary, the 3D self-supported core-shell Co_3O_4@$CoMoO_4$ NPFs electrode grown directly on Ni foam has been successfully synthesized through a stepwise hydrothermal method with outstanding pseudocapacitive performance. The high specific capacitance of 1902 F g^{-1}, the outstanding cycling stability, and the improved rate capability could be attributed the synergistic contribution from the two promising pseudocapacitive materials, Co_3O_4 and $CoMoO_4$, together with the merits of 3D self-supported core/shell nanopine forest arrays architecture showing attractive electrochemical behavior as electrode materials for pseudocapacitors. Solid state asymmetric and symmetric supercapacitors further deliver high specific energy and power densities and exhibit outstanding cycling life. We believe that the work presented here not only suggests the possibility to engineer Co_3O_4 and $CoMoO_4$ into promising electrode materials, but presents a new way to create hybrid electrode architectures for energy storage devices, wearable and portable electronics.

Acknowledgments

We thank National Natural Science Foundation of China (No. 51572058, 91216123, 51174063, 51502057, 51521001), National Basic Research Program of China (2013CB934103, 2012CB933003), the National Natural Science Fund for Distinguished Young Scholars (51425204), the Natural Science Foundation of Heilongjiang Province (E201436), the International Science & Technology Cooperation Program of China (2013DFR10630, 2015DFE52770) and Specialized Research Fund for the Doctoral Program of Higher Education (SRFDP 20132302110031).

Appendix A. Supplementary material

Supplementary data associated with this article can be found in the online version at http://dx.doi.org/10.1016/j.nanoen.2015.10.036.

References

[1] G.Q. Zhang, H.B. Wu, H.E. Hoster, M.B. Chan-Park, X.W. Lou, Energy Environ. Sci. 5 (2012) 9453.
[2] P.H. Yang, Y. Ding, Z.Y. Lin, Z.W. Chen, Y.Z. Li, P.F. Qiang, M. Ebrahimi, W.J. Mai, C.P. Wong, Z.L. Wang, Nano Lett. 14 (2014) 731–736.
[3] C. Guan, X.H. Xia, N. Meng, Z.Y. Zeng, X.H. Cao, C. Soci, H. Zhang, H.J. Fan, Energy Environ. Sci., 5, 9085.
[4] P. Simon, Y. Gogotsi, Nat. Mater. 7 (2008) 845–854.
[5] M.S. Dresselhaus, I.L. Thomas, Nature 414 (2001) 332.
[6] S. Chu, A. Majumdar, Nature 488 (2012) 294.
[7] H.L. Wang, H.J. Dai, Soc. Rev 42 (2013) 3088.

[8] J.R. Miller, P. Simon, Science 321 (2008) 651–652.
[9] Y. Zhu, S. Murali, M.D. Stoller, K.J. Ganesh, W. Cai, P.J. Ferreira, A. Pirkle, R.M. Wallace, K.A. Cychosz, M. Thommes, D. Su, E.A. Stach, R.S. Ruoff, Science 332 (2011) 1537.
[10] Y.G. Zhu, Y. Wang, Y.M. Shi, J.I. Wong, H.Y. Yang, Nano Energy 3 (2014) 46–54.
[11] Y.F. Zhang, M.Z. Ma, J. Yang, H.Q. Su, W. Huang, X.C. Dong, Nanoscale 6 (2014) 4303.
[12] X.Z. Yu, B.G. Lu, Z. Xu, Adv. Mater. 26 (2014) 1044.
[13] H. Chen, L.F. Hu, Y. Yan, R.C. Che, M. Chen, L.M. Wu, Adv. Energy Mater. 3 (2013) 1636.
[14] J.P. Liu, J. Jiang, C.W. Cheng, H.X. Li, J.X. Zhang, H. Gong, H. J. Fan, Adv. Mater. 23 (2011) 2076.
[15] J. Chmiola, G. Yushin, Y. Gogotsi, C. Portet, P. Simon, P. L. Taberna, Science 313 (2006) 1760.
[16] A.S. Arico, P. Bruce, B. Scrosati, J.M. Tarascon, W. van Schalkwijk, Nat. Mater. 4 (2005) 366.
[17] K. Deori, S.K. Ujjain, R.K. Sharma, S. Deka, ACS Appl. Mater. Interfaces 5 (2013) 10665.
[18] M. Inagaki, H. Konno, O. Tanaike, J. Power Sources 195 (2010) 7880.
[19] C.Q. Shang, S. Dong, S. Wang, D.D. Xiao, P.X. Han, X.G. Wang, G. Lin, G.L. Cui, ACS Nano 7 (2013) 5430.
[20] C. Zhou, Y.W. Zhang, Y.Y. Li, J.P. Liu, Nano Lett. 13 (2013) 2078.
[21] C.Z. Yuan, J.Y. Li, L.R. Hou, X.G. Zhang, L.F. Shen, X.W. Lou, Adv. Funct. Mater. 22 (2012) 4592.
[22] J. Xu, Q.F. Wang, X.W. Wang, Q.Y. Xiang, B. Liang, Di Chen, G. Z. Shen, ACS Nano 7 (2013) 5453.
[23] D.Z. Kong, J.S. Luo, Y.L. Wang, W.N. Ren, T. Yu, Y.S. Luo, Y. P. Yang, C.W. Cheng, Adv. Funct. Mater. 24 (2014) 3815.
[24] K.M. Hercule, Q.L. Wei, A.M. Khan, Y.L. Zhao, X.C. Tian, L. Q. Mai, Nano Lett. 13 (2013) 5685.
[25] K.W. Qiu, Y. Lu, D.Y. Zhang, J.B. Cheng, H.L. Yan, J.Y. Xu, X. M. Liu, J.K. Kim, Y.S. Luo, Nano Energy 11 (2015) 687.
[26] H. Zhang, G.P. Cao, Z.Y. Wang, Y.S. Yang, Z.J. Shi, Z.N. Gu, Nano Lett. 8 (2008) 2664.
[27] X.X. Qing, S.Q. Liu, K.L. Huang, K.Z. Lv, Y.P. Yang, Z.G. Lu, D. Fang, X.X. Liang, Electrochim. Acta 56 (2011) 4985.
[28] X.H. Xia, J.P. Tu, Y.J. Mai, X.L. Wang, C.D. Gu, X.B. Zhao, J. Mater. Chem. 21 (2011) 9319.
[29] L.Q. Mai, F. Yang, Y.-L. Zhao, X. Xu, L. Xu, Y.-Z. Luo, Nat. Commun. 2 (2011) 381.
[30] X. Xia, W. Lei, Q. Hao, W. Wang, X. Wang, Electrochim. Acta 99 (2013) 253–261.
[31] M.C. Liu, L.B. Kong, C. Lu, X.J. Ma, X.M. Li, Y.C. Luo, L. Kang, J. Mater. Chem. A 1 (2013) 1380.
[32] D. Guo, H.M. Zhang, X.Z. Yu, M. Zhang, P. Zhang, Q.H. Li, T. H. Wang, J. Mater. Chem. A 1 (2013) 7247.
[33] Z.X. Gu, R.F. Wang, H.H. Nan, B.Y. Geng, X.J. Zhang, J. Mater. Chem. A 3 (2015) 14578–14584.
[34] T. Zhu, J.S. Chen, X.W. Lou, J. Mater. Chem. 20 (2010) 7015–7020.
[35] B.L. Ellis, P. Knauth, T. Djenizian, Adv. Mater. 26 (2014) 3368.
[36] K. Liang, X.Z. Tang, W.C. Hu, J. Mater. Chem. 22 (2012) 11062.
[37] R.N. Singh, M. Hamdani, J.F. Koenig, G. Poillerat, J.L. Gautier, P. Chartier, J. Appl. Electrochem. 20 (1990) 442.
[38] Y.Q. Wu, X.Y. Chen, P.T. Ji, Q.Q. Zhou, Electrochim. Acta 56 (2011) 7517.
[39] Y. Gao, L.W. Mi, W.T. Wei, S.Z. Cui, Z. Zheng, H.W. Hou, ACS Appl. Mater. Interfaces 7 (2015) 4311.
[40] K. Wang, C.G. Zhao, S.D. Min, X.Z. Qian, Electrochim. Acta 165 (2015) 314.
[41] R.L. Liang, H.Q. Cao, D. Qian, Chem. Commun. 47 (2011) 10305.
[42] L. Zheng, Y. Xu, D. Jin, Y. Xie, J. Mater. Chem. 20 (2010) 7135.
[43] R. Ramkumar, M. Minakshi, Dalton Trans. 44 (2015) 6158–6168.
[44] J.W. Lang, L.B. Kong, M. Liu, Y.C. Luo, L. Kang, J. Solid State Electrochem. 14 (2010) 1533.
[45] Z. Tang, C.H. Tang, H. Gong, Adv. Funct. Mater. 22 (2012) 1272.
[46] P.H. Yang, W.J. Mai, Nano Energy 8 (2014) 274–290.

Jing Wang received her bachelor degree from School of Chemistry and Chemical Engineering at Qiqihar University, China in 2011. And received her master degree in Inorganic Chemistry at Harbin Normal University in 2013. She is currently a Ph.D. candidate under supervision of Prof. Jiupeng Zhao at School of Chemical Engineering and Technology, Harbin Institute of Technology. Her research interests mainly focus on design, synthesis, and electrochemical properties of transition metal oxide nanostructures.

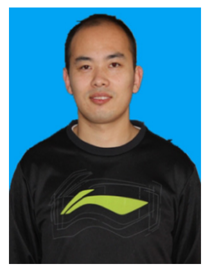

Xiang Zhang received his B.S. degree in Materials Science and Engineering from Zhengzhou University in 2010. He received his M.S. degree in Materials Engineering from Guangxi University. He is a doctoral candidate majoring in Materials Science and Engineering at Center for Composite Materials of Harbin Institute of Technology since 2015. His research interests mainly concern the design, synthesis, and characterization of photoelectric material and energy storage material.

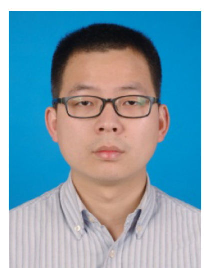

Qiulong Wei received his B.S. degree in Department of Materials Science and Engineering from Wuhan University of Technology in 2011. He has joined State Key Laboratory of Advanced Technology for Materials Synthesis and Processing for four years. He is currently working toward the Ph.D. degree. His current research involves the design and synthesis of nanomaterials for achieving both high energy density and power density electrochemical energy storage device, including the lithium-ion battery, sodium ion battery and the hybrid capacitor.

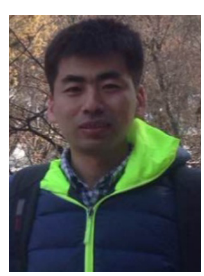

Haiming Lv is a Ph.D. student at Center for Composite Material, Harbin Institute of Technology. He received his B.S at Inner Mongolia University For The Nationalities and M.S at JiLin University. His research focuses mainly on nanomaterials for electrochromic application.

Yanlong Tian received his B.S. degree in chemistry from Taiyuan Normal University in 2010. He received his M. S. degree in applied chemistry from Zhejiang Sci-Tech University. He is a doctoral candidate majoring in Materials Science and Engineering at Center for Composite Materials of Harbin Institute of Technology since 2014. His research interests mainly concern preparation and investigation of inorganic functional materials for energy storage and conversion applications, including: porous, photocatalytic, and electrochromic materials.

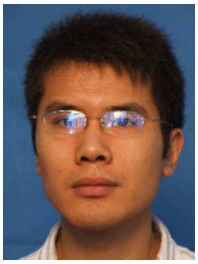

Zhongqiu Tong received his B.S. degree in Material Chemistry from Harbin Engineering University in 2010 and he is currently working toward the Ph.D degree in Materials Science at Harbin Institute of Technology. His current research is the preparation of 1D nanostructured vanadium pentoxide materials from three-dimensionally ordered macroporous vanadium pentoxide film.

Xusong Liu received his bachelor degree from College of Chemistry and Chemical Engineering at Qiqihar University, China in 2005. He is currently a Ph.D. candidate under supervision of Prof. Jiupeng Zhao at School of Chemical Engineering and Technology, Harbin Institute of Technology. His research interests mainly focus on design, fabrication, application and characterization of 1D Ge-based materials for Li ion battery.

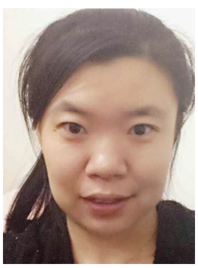

Jian Hao is currently a PhD student at Harbin Institute Technology (HIT). She received her master degree from Heilongjiang University in 2011. Her research interests include semiconductor nanomaterials (Ge and Si) and carbon nanomaterials, electrodeposition in ionic liquid and the applcations in energy storage.

Huiying Qu is a Ph.D. student majored in Chemical Engineering and Technology. She received her B.S. at Harbin Institute of Technology. Her research focuses mainly on transition-metal oxides for electrochromism.

Jiupeng Zhao received her Ph.D. degree from Harbin Institute of Technology (HIT) in 2000. She has been a Professor in the School of Chemical Engineering and Technology at HIT since 2007. Her research is focusing on the design and fabrication of nanostructured materials for energy storage applications and electrical devices.

Yao Li has been a Professor of Materials Science in Harbin Institute of Technology (HIT) since 2005 and leads the laboratory of Functional Composite Materials. He received the Ph.D. degree from HIT in 2000. He is the author or co-author of over 100 papers, 35 patents, and two. His research interests include fabrication and engineering nanostructured materials with well-defined microstructure and multiple length scales, and their applications for energy storage, electrochromism and photonic crystals. He was selected in “New Century Excellent Talents program”, “Distinguished Young Scholars for the Heilongjiang Province”. He was awarded “Science and Technology Award for the Youth of China”, “National Award of the Outstanding Scientific and Technological Workers” and “the First Prize for Heilongjiang Natural Science ”.

Liqiang Mai is Chair Professor of Materials Science and Engineering at Wuhan University of Technology (WUT) and Executive Dean of International School of Materials Science and Engineering at WUT. He received his Ph.D. from WUT in 2004. He carried out his postdoctoral research in the laboratory of Prof. Zhonglin Wang at Georgia Institute of Technology in 2006–2007 and worked as advanced research scholar in the laboratory of Prof. Charles M. Lieber at Harvard University in 2008–2011. His current research interests focus on nanowire materials and devices for energy storage. He received the National Natural Science Fund for Distinguished Young Scholars, the First Prize for Hubei Natural Science Award and so forth.